Advanced Materials Technologies

ADVANCED MATERIALS TECHNOLOGIES
www.advmattechnol.com

RESEARCH ARTICLE OPEN ACCESS

Unveiling Complementary Unipolar Electrical Transport in ZnO-Co_3O_4 Core–Shell Nanowires Exploiting Iontronics

Valeria Demontis[1] | Mojtaba Gilzad Kohan[2] | Luca Nappi[3] | Maria Jesus Rodriguez Douton[4] | Alberto Vomiero[2,5] | Francesco Rossella[3]

[1]Department of Physics, University of Cagliari, Monserrato, Italy | [2]Division of Materials Science, Department of Engineering Sciences and Mathematics, Luleå University of Technology, Luleå, Sweden | [3]Department of Physics, Informatics and Mathematics, University of Modena and Reggio Emilia, Modena, Italy | [4]"Engineering Department "Enzo Ferrari", University of Modena and Reggio Emilia, Modena, Italy | [5]Department of Molecular Sciences and Nanosystems, Ca' Foscari University of Venice, Venezia, Mestre, Italy

Correspondence: Francesco Rossella (francesco.rossella@unimore.it)

Received: 8 July 2025 | **Revised:** 25 October 2025 | **Accepted:** 3 November 2025

Keywords: core–shell nanowires | electronic transport | iontronics | metal oxide heterojunctions

ABSTRACT

Metal oxide heterostructure assemblies made of ZnO-Co_3O_4 core–shell nanowires enable high-performance self-powered optoelectronic devices with potential applications in wireless, autonomous, low maintenance medical implants or environmental sensors. Surprisingly, the experimental study of the single core–shell heterostructures forming the assembly was never reported until now. We unveil the transport phenomena occurring in individual ZnO-Co_3O_4 core–shell nanowires by engineering ionic liquid-gated nanotransistors. The nanostructures are isolated on fabrication substrates and equipped with a set of metallic electrodes probing selectively different sections of the nanowire, in three different configurations labelled core–core, shell–shell and core–shell. The observed electrical responses reflect the properties of the ZnO core, the Co shell and the core–shell heterojunction. The ultrahigh capacitive coupling of the ionic liquid to the nanowire and its conformal feature reveal multiple transport regimes in the same nanodevice: the core, the shell and the core–shell heterojunction act as a linear, nonlinear, and rectifying nanoelectronic components, respectively. This work shines light on the transport properties of individual metal oxide nanowire heterostructures employed in self-powered optoelectronics, suggesting potential applications as multifunctional nanoelectronic components. The methodologies developed in this research set the benchmark for the investigation of nanoscale building blocks of functional semiconductor nanomaterial assemblies for electronic and optoelectronic applications.

1 | Introduction

The availability of novel hardware devices such as sustainable, efficient and affordable self-powered sensors, wearable and wireless devices and healthcare implants, is essential to unlocking the full potential of the top trending cutting-edge technologies such as augmented reality, Internet of Things, advanced robotics and personalized medicine. Among the material families potentially suitable for these applications, metal oxide (MO_x) semiconductor nanostructures stand out as a potential alternative to silicon [1, 2] due to their unique combination of electrical and optical properties, abundance in nature, high thermal and chemical stability, non-toxicity and cost-effectiveness. MO_x materials represent, for instance, an ideal platform for electronic and optoelectronic devices, solar cells, photodetectors, and sensors operating under various environmental conditions [3, 4], thanks to their wide range of bandgaps supporting light absorption in a broad spectrum ranging from UV–vis to infrared (IR), coupled to interesting electronic properties at the nanoscale [5].

MO_x nanostructures with large aspect ratio - quasi 1D materials - exhibit enhanced properties compared to their bulk counterparts [6]: the high specific surface area facilitates extensive interaction with the external environment [3], while the high aspect ratio [7] might enable effective tuning of electronic properties through field effect mechanisms, particularly in the case of all-around gate geometries implemented via ionic liquid gating [8–11]. In this context, the ZnO system is applied in various fields of physics and technology [12–14] and increases interest in the nanoscience and technology community [15–17]. In particular, ZnO nanowires (NWs) provide a mature nanotechnology platform, with well-developed growth processes and extensively investigated properties [18]. They are typically n-type materials with a wurtzite crystal structure and a large direct bandgap of 3.37 eV at room temperature [19]. Notably, considerable research efforts currently aim at developing heterojunctions based on ZnO, in order to create all-MO_x-based functional devices. To this end, several oxides are being investigated as p-type absorbers and cuprous oxide, with a bandgap of 2 eV, is among the most relevant [20, 21].

Among ZnO-based NW systems, a novel type of quasi 1D core–shell heterostructure is emerging, with the ZnO nanowire (NW) core n-type conformally surrounded by the p-type Co_3O_4 shell [22, 23], engineering a radial ZnO/Co_3O_4 heterojunction along the NW axis. Even in bulk and thin films, this heterojunction has proven an outstanding electro–optical response [22, 24, 25], where Co_3O_4 act as a p-type absorber with two direct bandgaps at 1.5 and 2.2 eV, allowing coverage of a wide spectral range from infrared to visible [26], and with a favorable band alignment with ZnO, promoting charge carrier separation [27, 28]. At the nanoscale, the heterojunction offers even better performance, thanks to the shorter distances that carriers have to travel before collection, reducing the probability of charge recombination. Additionally, in the NW architecture, the large aspect ratio provides a significantly large surface area available for absorption, while requiring less material. In this framework, densely packed arrays of ZnO-Co_3O_4 core–shell NWs have been used for self-powered photodetectors: the array was grown on conductive glass with fluorine-doped tin oxide, which serves as the front contact of the device, while the back of the array was electrically contacted by a thin layer of sputtered gol [22, 23]. Remarkably, despite the exciting perspectives for the application of this new family of nanostructured systems, the experimental study of the electrical transport properties of their individual building blocks still represents a formidable challenge, both at the scientific and nanotechnological levels, and has never been tackled up to now.

In this work, we started from a ZnO-Co_3O_4 core–shell NW array and, rather than focusing on the collective electrical response of the entire array, we used nanomanipulation and nanofabrication techniques to isolate individual core–shell NWs and use them to engineer nanoscale devices. This approach allowed us to experimentally address the electrical transport phenomena occurring in nanoscale multifunctional devices based on quasi- 1D MO_x core–shell heterostructures, with the n-type ZnO nanowire (NW) core conformally surrounded by the p-type Co_3O_4 shell. Specifically, individual NWs were selectively removed from the grown matrix using nanomanipulators and isolated onto a Si^{++}/SiO_2 substrate. Accurate scanning microscopy imaging allowed us to discriminate between NW sections where the ZnO core was exposed and NW portions where the core was covered by the Co_3O_4 shell. A comb of metal nanoelectrodes was then realized by electron beam lithography along the entire length of the heterostructure body, with a geometry enabling the probing of electric transport in three different measurement configurations, hereby referred to as “core–core” (C–C), “core–shell” (C–S), and “shell–shell” (S–S). This architecture implements a multifunctional electronic device: the core–core electrode configuration performs as a nanoscale ZnO field effect transistor, the core–shell configuration behaves as an all-oxide-based pn junction nanodiode suitable for operation as a photodetector, and the shell–shell configuration returns the electrical response of a two-terminal device with two Schottky contacts. The nanowire core (shell) exhibits transport properties characteristic of a linear (non-linear) n-type (p-type) electronic component, while the core–shell junction acts as a rectifying element. In other words, each of the three sections of the nanowire probed in our transport experiment behaves as an independent, well defined unipolar electrical component: the core, as an n type semiconductor (ZnO); the shell, as a p type semiconductor (Co_3O_4), the section including the core–shell radial interface, as a p-n junction realized within a semiconductor material (ZnO-Co_3O_4 radial heterostructure).

Notably, in all three measurement configurations, conventional solid-state back-gate induces fairly poor field-effect modulation of electrical conductivity. To investigate the nature of charge carriers involved in transport mechanisms and to explore field-effect-induced modifications in transport behavior, we resorted to iontronics and in particular, to ionic liquid gating [8, 9, 29, 30], a technique that has shown superior performance compared to the standard solid-state back gates in tuning the electronic properties of nanostructures with large aspect ratio. Iontronics science and technology include all systems and methodologies associated to the use of mobile ions -their arrangement and movement- for controlling electronic devices [29]. Systems for iontronics include ionic liquids (molten salts at room temperature), gels [31], polyelectrolytes [11] and even solid electrolytes [32]. Iontronic methodologies encompass any technique suitable for building and controlling electric-double-layers (EDLs) at the interface between the ionic system and the active device channel: EDLs generate ultrahigh electric fields which modulate electrical currents in the devices. The combination of iontronic techniques and nanoscale semiconductor devices has shown superior performance compared to standard solid-state back-gates in tuning the electronic properties of nanostructures with large aspect ratio [8, 9, 30, 33].

Thanks to the iontronic gating, we observe device-level coexistence of both electron and hole channels within the same nanostructure, as well as the selective addressability of each channel. Our results demonstrate complementary n- and p-type conduction in distinct sections of the same individual core–shell nanowire, i.e., ambipolar functionality at the device level. For sake of completeness, we notice that while our work focuses on core–shell metal–oxide nanowires and their multifunctional response, considerable work has been reported on the optical/photonic analogues of our system, enabling photonic and optical logic functionalities associated with the occurrence of ambipolar transport features. These include, for instance, self-assemblies of branched organic crystals [34], systems for

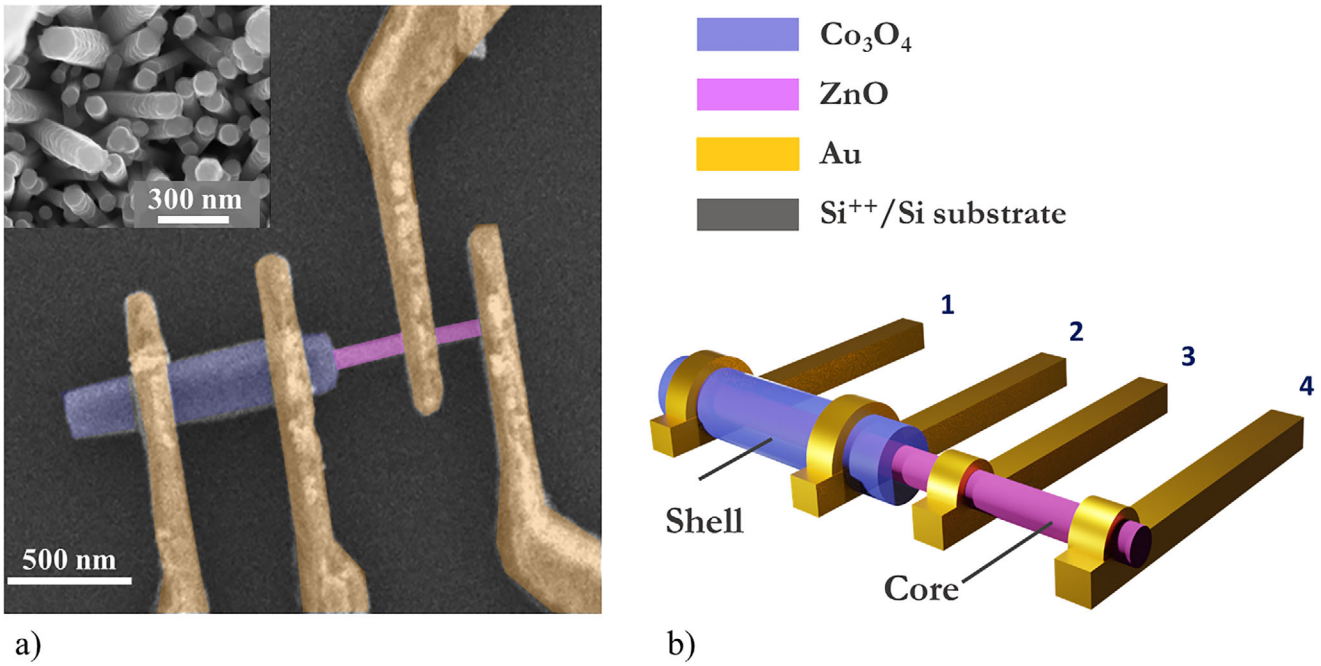

FIGURE 1 | (a) False colored top-view scanning electron micrograph of one of the electronic nanodevices fabricated starting from an individual ZnO-Co_3O_4 core–shell nanowire. The nanowire core (shell) is pink (blue) colored, metallized electrodes are yellow colored. Fabrication substrate is heavily p-doped Si/SiO2 substrate, with SiO_2 thickness of 300 nm. Inset: scanning electron micrograph of the as-grown core–shell nanowire array. (b) Pictorial representation of the device, equipped with a comb of four metal contacts, enabling two- probe measurements in three device configurations: core–core (leads 3-4), shell–shell (leads 1-2) and core–shell (leads 2-3).

the hierarchical integration of organic core/shell microwires for advanced photonics [35, 36] and branched homostructures displaying asymmetric optical waveguiding, suitable for operation as optical logic gates [37].

Compared with these materials, oxide nanowires are attractive for the chemical stability, nontoxicity, and abundance, providing an excellent material platform for optoelectronic device manufacturing under ambient condition [22]. In general, it is worth noting that the realization of devices based on metal oxides p-n junction is quite challenging, due to the difficulty of finding suitable p-type materials (e.g., difficulty in p-type doping in ZnO [38]) and due to the relatively low mobility of the charge carrier in most of the metal oxides [22].

Our work discloses the nanoscale transport phenomena behind the operation of self-powered devices based on metal oxide nanostructures, experimentally addressing the building blocks consisting of individual ZnO-Co_3O_4 core–shell nanowires. In addition, the three different transport behaviors associated with different measurement configurations of the same nanodevice might be exploited for the development of multifunctional electronic components for microscale/nanoscale circuitry.

2 | Results and Discussion

Figure 1 illustrates the different preliminary steps of the transport experiments. In particular, Figure 1a shows a false color top view scanning electron micrograph of one of the devices investigated, while the inset reports a scanning electron micrograph of the as-grown core–shell NW array. The ZnO NW core is colored pink, the Co_3O_4 shell in violet, and the Cr/Au electrical contacts (10 nm/100 nm) yellow. Figure 1b shows a pictorial representation of the device architecture. The electrodes are labeled 1 to 4 and allow multiple measurement configurations: S–S configuration (contact pairs 1–2), C–S configuration (contact pairs 2–3), and C–C configuration (contact pairs 3–4).

The two-terminal current–voltage (I_{ds}–V_{ds}) characteristics of the device in the three measurement configurations, at room temperature under a controlled pressure of 10^{-6}mbar in dark, were first investigated. Figure 2 reports the experimental results as three different curves, I_{ds}–V_{ds}. In the C–C configuration, electrical transport occurs throughout the ZnO NW core, between contacts 3 and 4 (Figure 2a). The characteristic I_{ds}–V_{ds} (Figure 2d) is linear, indicating the formation of good ohmic contacts at the semiconductor/metal interface and an electrical resistivity of approximately 0.7 Ω cm, consistent with previous reports on ZnO NWs with similar diameter [39]. In this configuration, the expected zero bias energy band diagram is shown in Figure 2g and corresponds to a semiconductor material of type n with injection contacts at the semiconductor/metal interfaces. Notably, here, ohmic contacts in ZnO nanostructures are obtained using metals commonly used in nano- and microfabrication processing and without any additional surface treatment: this represented a challenging task [40, 41] and chromium as an ohmic contact to ZnO thin film has been only recently reported [42].

In the S–S configuration (Figure 2b), electrical transport in the Co_3O_4 shell is probed. The experimental I_{ds}–V_{ds} characteristic

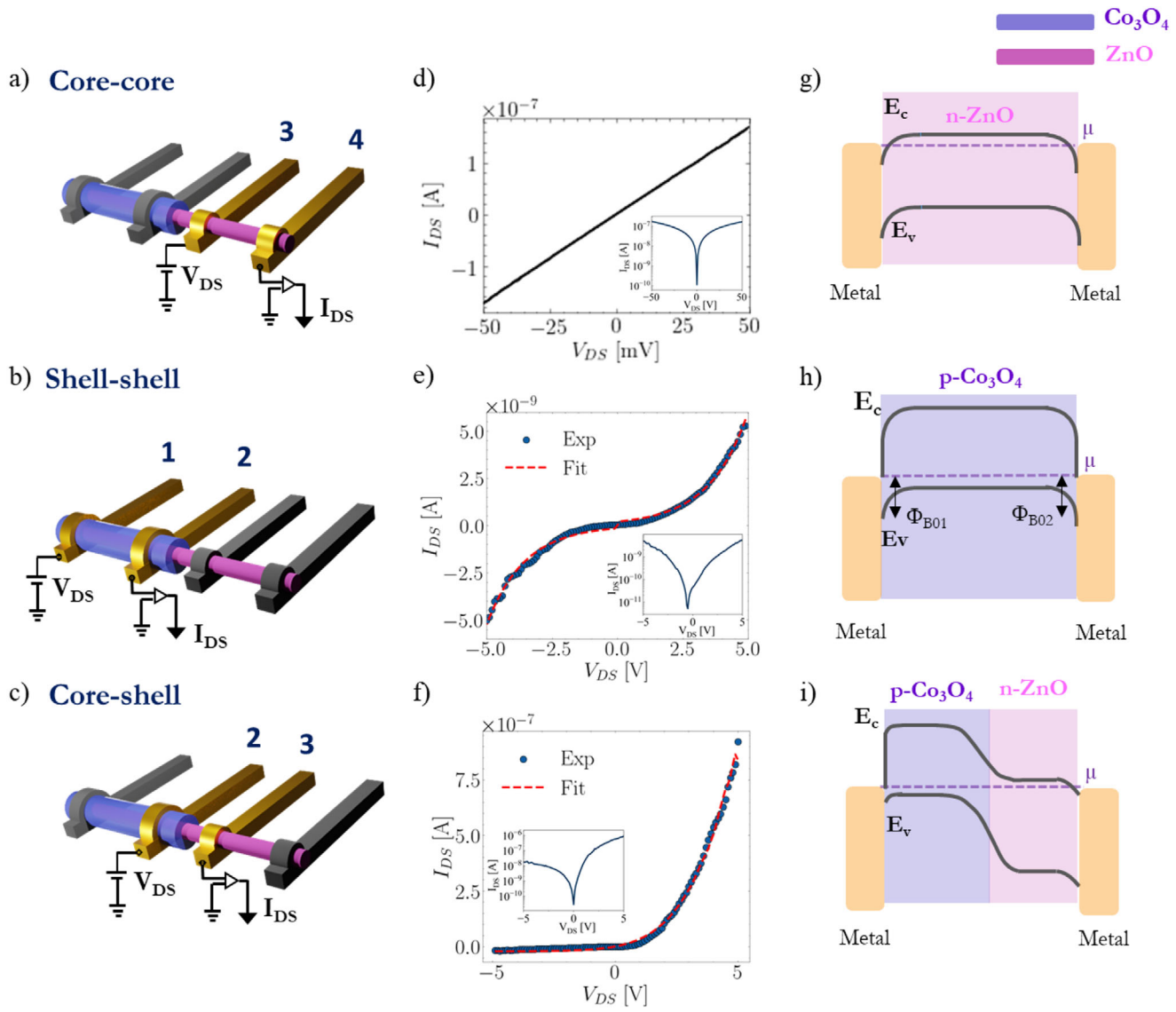

FIGURE 2 | Electric circuit configuration (in overlay) for the core–core (C–C) configuration (a), for the shell–shell (S–S) configuration (b) and for the core–shell (C–S) configuration (c). Two-probe I_{ds}-V_{ds} characteristic measured in the C–C configuration (d), in the S–S configuration (e) and in the core–shell configuration (f). Insets in panels (d–f) display the semi log-scale plots of the *I-V* curves. Dashed red lines in e) and f) are fits to a double Schottky barrier device response and a pn junction diode, respectively. Energy band diagrams for the unbiased condition: C–C (g), S–S (h) and C–S (i). E_c and E_v denote conduction-band minimum and valence-band maximum, respectively; mu is the electrochemical potential, and Φ_{B01} and Φ_{B02} in (h) are the Schottky barriers heights at the metal/Co_3O_4 interface.

(blue dotted line in Figure 2e is symmetric to both positive and negative voltage sweeps, but exhibits a strongly non-linear behavior, with electrical resistivity (extracted from the high bias regimes) of approximately 900 Ωcm, i.e., much larger with respect to the core. This strongly suggests the presence of Schottky barriers with similar heights at both electrical contacts [43], increasing contact resistance and reducing current levels. Figure 2h shows the band diagram of the device in a shell–shell measurement configuration without applying an external bias. Barriers at the two contacts are denoted as ϕ_{B01} and ϕ_{B02}. Barrier heights can in general, be different, reflecting the morphological features of the interfaces and their overall quality. This suggests adopting a two-terminal device model with rectifying contacts [43] which assumes as equivalent circuit two back-to-back diodes separated by a series resistance, enabling the extraction of Schottky barrier heights and the ideality factor, which account for deviations of conduction from thermionic emission. Accordingly, the current in this system reads:

$$I = \frac{2I_{s_1}I_{s_2}sinh\left(\frac{qV}{2kT}\right)}{I_{s_1}e^{\frac{qV}{2kT}} + I_{s_2}e^{\frac{qV}{2kT}}} \quad (1)$$

where I_{s1} and I_{s2} are the reverse saturation currents, expressed as:

$$I_{s_1,s_2} = S_{1,2}A^*T^2exp\left(\frac{\phi_{B1,2}}{kT}\right) \quad (2)$$

$S_{1,2}$, A^*, T and k being the areas of the junctions, the Richardson constant, the temperature and the Boltzmann constant, respec-

tively. ϕ_{B1} and ϕ_{B1} are defined as the effective Schottky barriers and take into account the deviation from the ideality via the formula:

$$\phi_{B_1,B_2} = \phi_{B01,B02} \pm eV_{1,2}\left(1 - \frac{1}{n_{1,2}}\right) \quad (3)$$

ϕ_{B01}, ϕ_{B02}, $n_{1,2}$ are used as fit parameters. The fit curve is reported as the red dashed line superimposed on the experimental curve in Figure 2e. The extracted Schottky barriers values are similar, approximately 0.47 eV each, and both the ideality factors are around 1.02. The formation of Schottky barriers for hole conduction at the Cr/Co_3O_4 interface (Cr is used as an adhesion layer for metal contact fabrication, as shown in Methods) can be justified by the difference in the metal and semiconductor work functions, by resorting to the ideal Schottky–Mott theory for the contact between a metal and a semiconductor with higher work function (Co_3O_4 work function was estimated in the literature to be around 5.2 eV [44], while Cr work function is 4.5 eV [45]). In the literature, for Co_3O_4 NWs, non linear *I-V* characteristics were observed also in the case of favorable alignments of the work function (as in the case of Pt contacts, having a work function of 5.65 eV) [46]. These deviations from the expected behavior were attributed to other conduction mechanisms, such as Fermi-level pinning [47], space-charge-limited conduction, and phenomena related to intrinsic material properties. In our case, the ideality factors approximating 1 for both barriers suggest that we can consider thermionic emission as the dominant mechanism.

In the C–S configuration (Figure 2c), electrical transport through the ZnO-Co_3O_4 junction is probed. The output characteristics (Figure 2f) displays the clear rectifying behavior of a p-n junction diode, characterized by an exponentially increasing current in the forward voltage regime and by a small reverse current in the reverse voltage regime. The overall current intensity in this configuration is intermediate with respect to the other configurations. The output characteristics (Figure 2f) display the rectifying behavior characteristic of a p-n junction diode, with exponentially increasing current in the forward bias regime and small current in the reverse bias regime. Semi-logarithmic current plots indicate rectification ratios for the C–S configuration of 16 at ±2V bias voltage, increasing up to 53 at ±5 V bias. The same order of rectifications was reported for ensembles of oxide nanoscale p–n devices (ratios 10 at 1 V in ZnO-CuO [48]): in these disordered systems, extracting information on the single nanowire building block is barely impossible. Larger rectifications (exceeding 100) were reported only in the case of fully engineered interfaces in optimized material pairs [49]. Although rectification ratio in our systems is all but optimized and, likely, it is detrimentally affected by Schottky–limited contacts to the p-type shell, however, our finding represents the first direct experimental estimate of the electrical parameters (including rectification) of individual nanoscale heterojunctions implemented in core–shell all-oxide (ZnO-Co_3O_4) nanowires.

Regarding the leakage currents exhibited by the diode-like section of our nanodevices, currents in the 1–10 nA range (relatively high, sub-optimal) are typically observed.

Unbiased energy band diagrams reported in Figure 2i represent a schematic, not-to-scale illustrations of the transport mechanisms behind the three different transport responses observed in our device, useful for the qualitative rationalization of the experimental findings. While the n-type core forms ohmic contact with the metallic electrode, the p-type Co_3O_4 shell forms a Schottky barrier for holes. The experimental results are best fitted by the pn diode model with a series resistance, R_s:

$$I = I_s\left(e^{\frac{q(V+IR_S)}{nkT}} - 1\right) \quad (4)$$

I_s, n and R_s were used as fit parameters. The fit curve is reported as the red dashed line superimposed to the experimental curve in Figure 2f. The extracted value of the series resistance is about 1 MΩ, relatively high most likely due to the poor quality of the electrical contact at the Co_3O_4 shell.

The Si^{++}/SiO_2 substrate was voltage-polarized through the highly doped silicon substrate and was used as a backgate to investigate device operation as a field effect transistor (Figure 3a). With this approach, each device configuration (C–C, C–S, and S–S) was tested upon application of the back-gate voltage, V_{BG}, and very poor or negligible modulation of the current was observed (Figure 3b–d, black curves). As for the core–core configuration (Figure 3b), for applied V_{BG} in the range from +30 to –30V, just a few per cent modulation of the current is observed, with an estimated field-effect mobility of a few cm^2/Vs. In both core–shell (Figure 3c) and core– core (Figure 3d) configurations, the poor efficiency of the back-gate is further reduced by the system's geometry. The exposed portion of the core, in fact, is not in direct contact with the substrate but is suspended at a few tens of nanometers, corresponding to the shell thickness of the adjacent segment.

To overcome these limitations of the conventional field effect approach and fully disclose the electrical transport properties of the investigated nanomaterials, a different approach based on iontronics was adopted, using an ionic liquid as the electrolyte gating medium. Ionic liquids are salts, melted at 300K, consisting of a charge-neutral ensemble of positive and negative ions: they are electronic insulators but ionic conductors, where ions can drift in response to a temperature [11] or a voltage gradient [50]. When an ionic liquid, in contact with a semiconductor, is voltage polarized, e.g. by applying a voltage to a metallic element plunged in the liquid, ions of one sign tend to accumulate at the liquid/semiconductor interface, while ions of the opposite sign tend to accumulate at the liquid/metal interface. For positive (negative) ion accumulation onto the surface of an n-type (p-type) semiconductor, a positive (negative) charged layer builds up, inducing the accumulation of an electron (hole) layer in the semiconductor. These two opposite charge distributions at the nanometer scale distance realize an electric double layer typically characterized by nanogap capacitance and an electric field exceptionally large, up to μF cm^{-2} and 100 MW/cm, respectively [8, 29]. The advantage of this approach, referred to as ionic liquid gating, is manifold: In addition to the ultra-high capacitive coupling with the semiconductor, it is fully compatible with room-temperature device operation (preserving the ionic system in the liquid state) and it provides conformal gating to the semiconductor, whatever its geometry, shape, and dimensions.

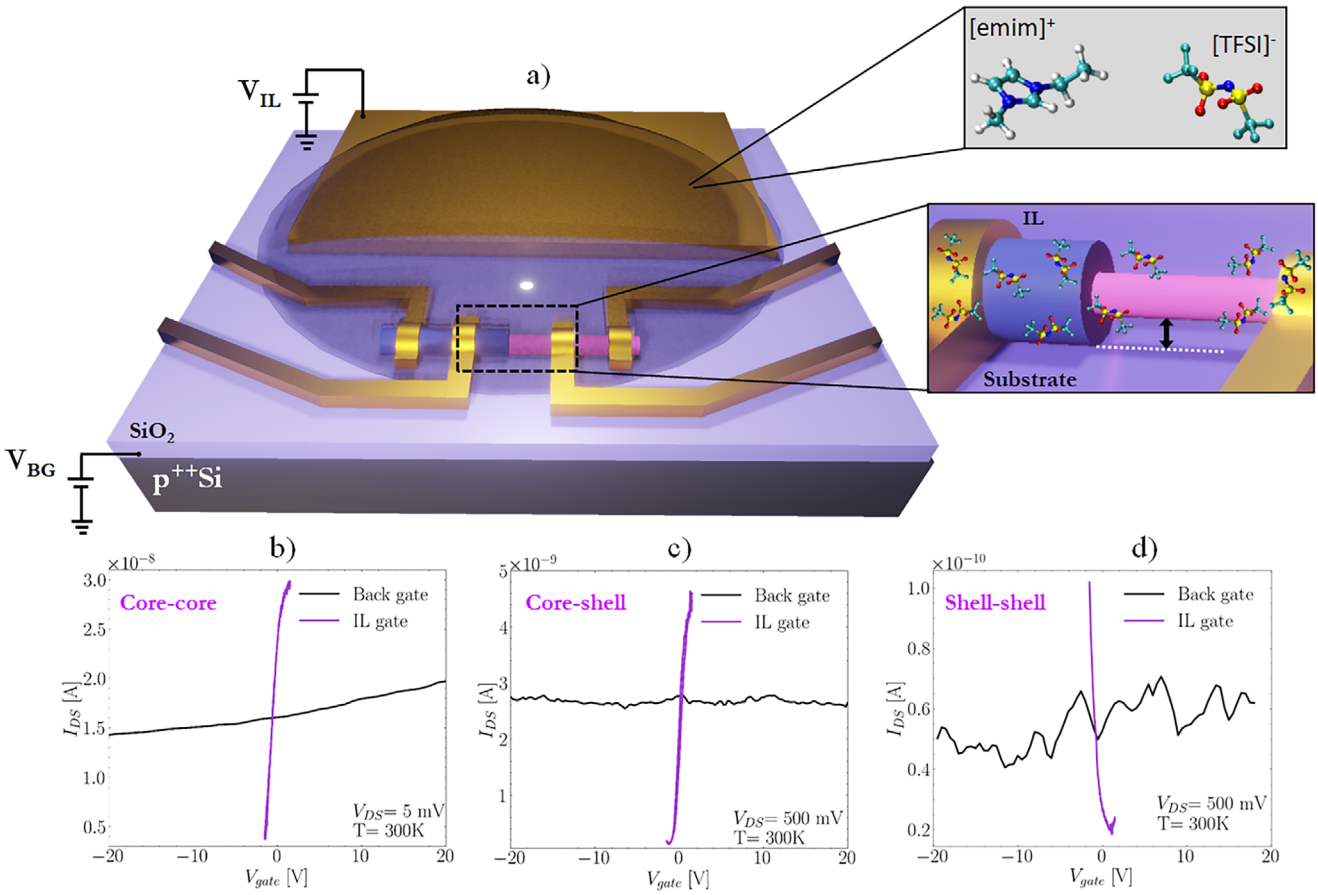

FIGURE 3 | (a) Schematic of the dual-gated device architecture. The device is embedded in a droplet of imidaziolium-based ionic liquid ([EMIM$^+$][TFSI$^-$]), consisting of positively and negatively charged ions as depicted in the top inset. A 100 μm^2 square electrode, fabricated at a few tens of μm from the nanodevice, can be voltage-polarized (V_{IL}) to control the spatial distribution of ions inside the ionic liquid surrounding the nanowire, as shown in the bottom inset. The Si/SiO_2 substrate acts as a back gate upon the application of V_{BG}. (b), (c) and (d) show the transfer characteristics measured as function of back-gate applied voltage (black lines) and ionic liquid gate voltage (purple lines) for the C–C, C–S and S–S configurations, respectively.

To perform the ionic-gating experiment, as pictorially represented in Figure 3a, the device was also equipped with a large metallic electrode (square shape, 100 μm side), realized in the same single step lithography used to fabricate the nanodevice. The ionic liquid is drop-casted and embeds the entire device, comprising the four-contact core–shell nanowire device and the gate electrode, thus the application of a voltage to the electrode drives ionic motion and arrangement. Imidaziolium-based ionic liquid, ([EMIM$^+$][TFSI$^-$]), was used, and the two ions that make up the liquid are depicted in the top inset of Figure 3a. Voltages in the range from –1.5 to +1.5 V were applied at room temperature to the large electrode to polarize the ionic liquid preserving its electrochemical stability [51]. The bottom inset in Figure 3a schematically depicts a detail of the ionic-gated nanowire device: mobile ions in the electrolyte, arrange conformally on the surface of each section of the nanowire, including the core, which is separated from the substrate and thus very poorly coupled to the capacitance of the silicon oxide layer. Figure 3b–d report the transfer characteristics measured against back gate voltage (black line) and ionic liquid gate voltage (pink line) for the three operations of the multifunctional device.

The ionic liquid, with its capacitive coupling to the semiconductor nanostructure, exceeding almost two orders of magnitude the nanowire-to-backgate coupling (from the rough estimation of transfer curve slopes), provides the key to full control of the device by field effect, as is reported in detail in Figure 4. Figure 4a–c show the transfer characteristics, i.e., the source-drain current, I_{ds}, vs. ionic liquid gate voltage, V_{IL}, measured at room temperature with an applied source-drain voltage bias of 5 mV for the C–C configuration and 500 mV for S–S and C–S configurations. C–C transfer curves in Figure 4a indicate a n-type semiconductor material. I_{ds} increases monotonically for increasing V_{IL}, semiconductor depletion and device off-state are achieved with a threshold voltage of approximately –1 V, On/Off current ratio exceeds 10^2, and negligible hysteresis is observed upon sweep direction reversal of V_{IL} for sweep rates below 2 mV/s. S–S transfer curves are shown in Figure 4b and indicate a p-type semiconductor material, with I_{ds} decreasing monotonically as V_{IL} increases. In this case, the current modulation does not exceed one order of magnitude. C–S transfer curves reported in Figure 4c are consistent with an overall n-type behavior of the investigated nanowire section, suggesting a dominant contribution of the n-type core. Figure 4d–f show the output

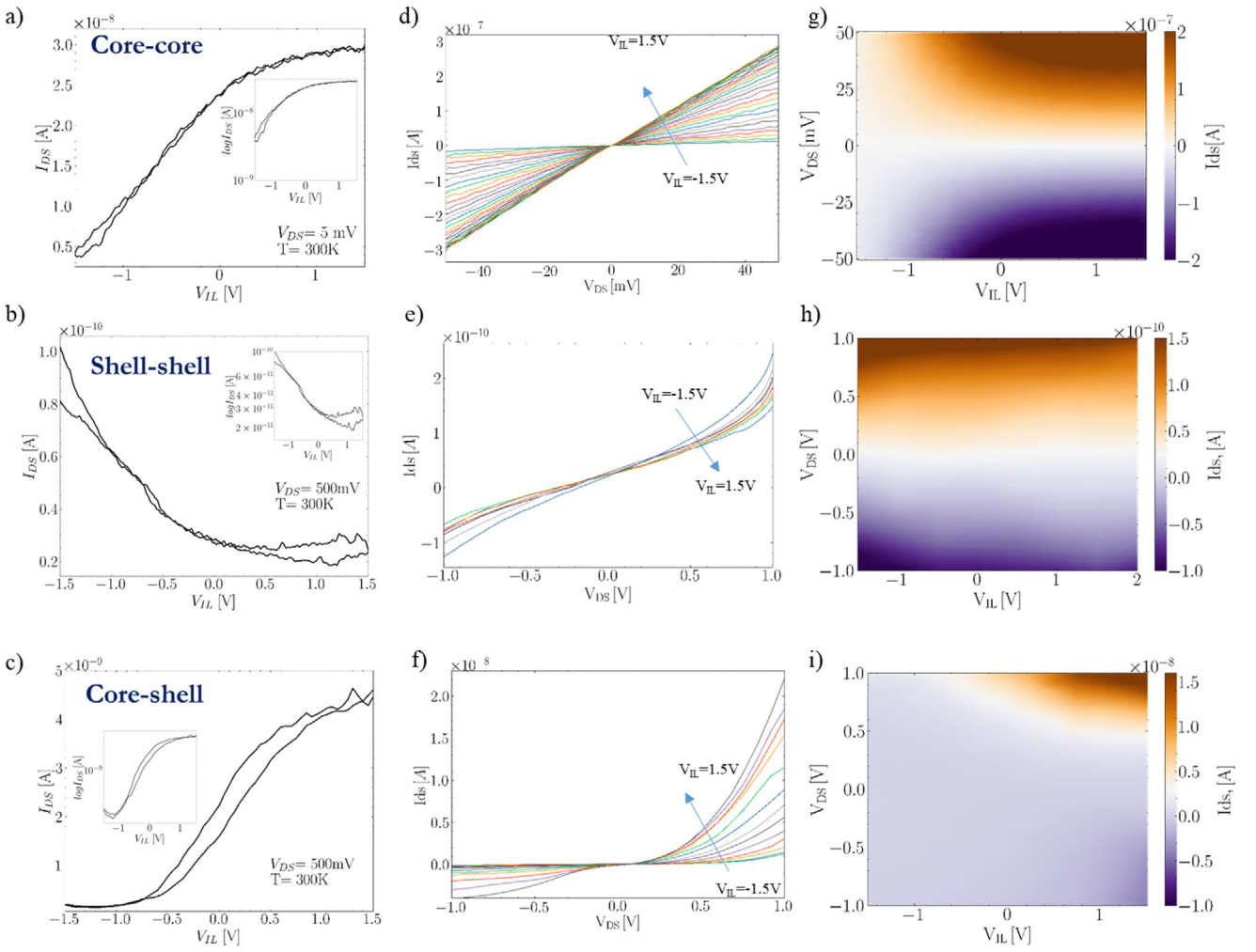

FIGURE 4 | Ionic liquid gated device operation. (a), (b) and (c): transfer curves vs. V_{IL} measured in the core–core, shell–shell and core–shell configuration, respectively (forward and reverse sweeps are shown; the inset display the transfer curves in semi-log scale). (d), (e) and (f): output characteristics (I_{ds} vs. V_{ds}) measured at different values of the applied ionic liquid gate voltage V_{IL} in the core–core, shell–shell and core–shell configuration, respectively. (g), (h) and (i): I_{ds} measured as a function of V_{ds} and V_{IL} for the three configurations.

characteristics, i.e. I_{ds} vs. V_{ds}, measured at room temperature with different applied V_{IL} for the device configurations as in panels (a–c), respectively. Finally, the color maps shown in Figure 4g–i report I_{ds} as a function of (V_{ds}) and V_{IL}, for the three different configurations.

It is worth noting that the multi-terminal device architecture engineered starting from an individual radial nanostructure (ZnO(core)/Co_3O_4(shell) nanowire) is functional to selectively address different sections of the nanostructure, each behaving as a specific electrical component. Using the pair of terminals (electrodes) labeled as "core" (C–C configuration measurement) it is possible to probe electrical transport in the ZnO core, resulting ohmic and n-type semiconductor-like. Using the two "shell" terminals (S–S configuration), electrical transport in the shell can be measured, revealing the occurrence of two back-to-back Schottky barriers at the metal-Co_3O_4 shell interface (symmetrical, non-linearity electrical response). Using the "core–shell" (C–S) configuration measurement, the radial p–n junction is probed, observing a rectifying behavior. In this frame, the ionic liquid used for electric-double-layer gating couples conformally to each section of the nanowire, the shell but also the core that, being separated by the substrate by the shell thickness, cannot be efficiently back-gated: iontronics thus enables the nanowire section-resolved electrostatic control of the device. The use of ion-gating applied to the nanoengineered multiterminal device architecture allows us to fully unveil the relation between the nanomaterial structure (heterostructure), the device architecture and the electrical response.

The experimental outcomes achieved with ionic liquid gating reveal transport regimes that were unattainable with back gating via the substrate. In particular, the iontronic approach unveiled the possibility of observing ambipolar transport in the device, with free electrons contributing to the electrical current across the ZnO core and holes transported in the Co_3O_4 shell. Furthermore, the low gate voltage operating range ($|V_{IL}| < 1.5\,V$) holds the potential for energy-efficient device operation. In addition, because device operation through ionic liquid gating does not depend on the type of substrate, one notable additional benefit of this approach is that it eliminates the necessity of fabricating devices on expensive wafers: device operation can

be accomplished using cost-effective substrates such as glass, plastics, paper or other flexible materials, thus opening the way to a wide range of low-cost applications.

3 | Conclusion

Using state-of-the-art nanotechnology tools for nanodevice fabrication and exploiting the emerging approach of iontronics for the field effect control of semiconductor nanomaterials, we experimentally demonstrate multiple transport phenomena occurring in individual ZnO-Co_3O_4 core–shell nanowires, building blocks for high-performance self-powered optoelectronic devices operating without the need for batteries or other external power sources. Prototypical device architectures developed for this work feature (i) a comb of four electrical contacts on single core–shell nanowires, with two contacts on the shell and two on the naked core, (ii) SiO_2/Si^{++} fabrication substrate, that can be operated as a back-gate, (iii) an ionic liquid droplet embedding the nanodevice and (iv) a large metallic electrode allowing to polarize the ionic liquid, operating it as an electrolyte gate. Electrical transport experiments are carried out by independently measuring the current flowing in the core, in the shell, and across the core–shell heterojunction, as a function of source-drain voltage bias and gate voltage. The nanowire core (shell) exhibits transport properties characteristic of a linear (non-linear) n-type (p-type) electronic component, while the core–shell junction acts as a rectifying element. Ambipolar electrical transport is thus revealed in this class of metal–oxide core–shell nanostructures. These can be used for developing innovative multifunctional electronic components characterized by low-gate voltage operation regime, thanks to the ultrahigh capacitive coupling between the semiconductor nanostructure and the ionic liquid electrolyte. To the best of our knowledge, this work provides the first report on the experimental measurement of electrical transport properties in individual ZnO-Co_3O_4 core–shell nanowire devices, selectively addressing the three different sub-structures (core, shell, core–shell junction) present in each single nanowire. In fact, the literature of the ZnO-Co_3O_4 and similar systems is limited to macroscale optoelectronic devices consisting of disordered assemblies of nanorods strongly interconnected: the planar areas and contact densities exhibited by such devices might differ by order of magnitudes from their single-nanowire counterparts. In other words, our work provides the actual benchmark for the investigated nanosystems.

4 | Experimental Section

4.1 | Synthesis

Single crystal wurtzite n-type ZnO NWs were synthesized by hydrothermal synthesis on silicon substrates [52]. A 0.1 M zinc acetate dehydrate in ethanol was spin-coated on the substrate as a seed layer for ZnO. The substrate was then annealed for 60 min in air, at 450°C. The seeded samples were then autoclaved with an aqueous solution of 100 mM of $Zn(NO_3)_2.6H_2O$ and 100 mM of hexamethylenetetramine (HMTA) and finally kept at 95°C for 3 h. The p-type Co_3O_4 shell was deposited on ZnO NWs by means of reactive DC magnetron sputtering using a pure cobalt target in a reacting atmosphere of 95% Argon and 5% Oxygen, at a deposition temperature of 300°C.

4.2 | Device Nanofabrication

After growth, the densely packed array of vertical ZnO/Co_3O_4 core–shell NWs was sonicated in isopropanol to mechanically remove the NWs from the growth substrate. Single NWs were then transferred by drop-casting on a Si^{++} substrate with a top SiO_2 insulating layer of 300 nm. The deposited NWs were then inspected by scanning electron microscope, and some of them, i.e. the ones with a suitable morphology, with core and shell segments clearly recognizable, were selected and manipulated (using manomanipulators insiede the scanning electron microscope) for device fabrication. A comb of metal leads of Cr (10nm), used as the adhesion layer, and Au (100 nm) was defined on each nanowire by means of aligned electron beam lithography, followed by thermal evaporation and lift-off.

Acknowledgements

V.D. acknowledges the funding from the Project "Network 4 Energy Sustainable Transition–NEST", Spoke 1, Project code PE0000021, funded by the European Union–NextGenerationEU under the National Recovery and Resilience Plan (NRRP), Mission 4, Component 2, Investment 1.3, Call for tender No. 1561 of 11.10.2022 from italian MUR and the funding of Bando Pubblico per lo sviluppo di Proof of Concept (PoC) Ecosistema dell–Innovazione e.INS - Ecosystem of Innovation for Next generation Sardinia (CUP F53C22000430001). FR acknowledges support from FAR 2024 Progetti interdisciplinari - Linea UNIMORE "NT-ROBOT" (CUP E93C24001920005) INFN project "MANIFOLD" National Recovery and Resilience Plan (PNRR), Mission 04, Component 2, Investment 1.5 NextGenerationEU, Call for tender No. 3277 dated December 30, 2021 (Award Number: 0001052 dated June 23, 2022).

Conflicts of Interest

The authors declare no conflicts of interest.

Data Availability Statement

The data that support the findings of this study are available from the corresponding author upon reasonable request.

References

1. L. Qiao, H. Y. Xiao, H. M. Meyer, J. N. Sun, C. M. Rouleau, A. A. Puretzky, et al., "Nature of the Bandgap and Origin of the Electro-/Photo-Activity of co3o4," *Journal of Materials Chemistry C* 1, no. 31 (2013): 4628, https://doi.org/10.1039/c3tc30861h.

2. E. Fortunato, P. Barquinha, and R. Martins, "Oxide Semiconductor Thin-Film Transistors: A Review of Recent Advances," *Advanced Materials* 24, no. 22 (May 2012): 2945–2986, https://doi.org/10.1002/adma.201103228.

3. B. Yang, N. V. Myung, and T.-T. Tran, "1D Metal Oxide Semiconductor Materials for Chemiresistive Gas Sensors: A Review," *Adv. Electron. Mater.* 7, no. 9 (Sept. 2021): 2100271.

4. I. Concina, Z. H. Ibupoto, and A. Vomiero, "Semiconducting Metal Oxide Nanostructures for Water Splitting and Photovoltaics," *Advanced Energy Materials* 7, no. 23 (2017): 1700706, https://onlinelibrary.wiley.com/doi/abs/10.1002/aenm.201700706.

5. Z. L. Wang, "Nanostructures of Zinc Oxide," *Materials Today* 7, no. 6 (June 2004): 26–33, https://doi.org/10.1016/s1369-7021(04)00286-x.

6. A. Zhang, G. Zheng, and C. M. Lieber, *Nanowires* (Springer International Publishing, 2016), https://doi.org/10.1007/978-3-319-41981-7.

7. F. Floris, L. Fornasari, V. Bellani, A. Marini, F. Banfi, and F. Marabelli, "Strong Modulations of Optical Reflectance in Tapered Core–Shell Nanowires," *Materials* 12, no. 21 (2019), https://www.mdpi.com/1996-1944/12/21/3572.

8. J. Lieb, V. Demontis, D. Prete, D. Ercolani, V. Zannier, and L. Sorba, "Ionic-Liquid Gating of InAs Nanowire-Based Field-Effect Transistors," *Advanced Functional Materials* 29, no. 3 Nov. 2018): 1804378, https://doi.org/10.1002/adfm.201804378.

9. D. Prete, V. Demontis, V. Zannier, M. J. Rodriguez-Douton, L. Guazzelli, and F. Beltram, "Impact of Electrostatic Doping on Carrier Concentration and Mobility in InAs Nanowires," *Nanotechnology* 32, no. 14 Jan. 2021): 145204, https://doi.org/10.1088/1361-6528/abd659.

10. D. Prete, E. Dimaggio, V. Demontis, V. Zannier, M. J. Rodriguez-Douton, and L. Guazzelli, "Electrostatic Control of the Thermoelectric Figure of Merit in Ion-Gated Nanotransistors," *Advanced Functional Materials* 31, no. 37 (July 2021): 2104175, https://doi.org/10.1002/adfm.202104175.

11. D. Prete, A. Colosimo, V. Demontis, L. Medda, V. Zannier, and L. Bellucci, "Heat-Driven Iontronic Nanotransistors," *Advanced Science* 10, no. 7 (Jan. 2023), https://doi.org/10.1002/advs.202204120.

12. Y.-C. Huang, J. Zhou, K. Nomenyo, R. E. Ionescu, A. Gokarna, and G. Lerondel, "Facile, Wafer-Scale Compatible Growth of ZnO Nanowires *via* Chemical Bath Deposition: Assessment of Zinc ion Contribution and Other Limiting Factors," *Nanoscale Advances* 2, no. 11 (2020): 5288–5295, https://doi.org/10.1039/d0na00434k.

13. S. Xu, Y. Qin, C. Xu, Y. Wei, R. Yang, and Z. L. Wang, "Self-Powered Nanowire Devices," *Nature Nanotechnology* 5, no. 5 Mar. 2010): 366–373, https://doi.org/10.1038/nnano.2010.46.

14. A. Vomiero, I. Concina, E. Comini, C. Soldano, M. Ferroni, and G. Faglia, "One-Dimensional Nanostructured Oxides for Thermoelectric Applications and Excitonic Solar Cells," *Nano Energy* 1, no. 3 (2012): 372–390, https://www.sciencedirect.com/science/article/pii/S221128551200078X.

15. H. Beitollahi, S. Tajik, F. G. Nejad, and M. Safaei, "Recent Advances in ZnO Nanostructure-Based Electrochemical Sensors and Biosensors," *Journal of Materials Chemistry B* 8, no. 27 (2020): 5826–5844, https://doi.org/10.1039/d0tb00569j.

16. L. Schmidt-Mende and J. L. MacManus-Driscoll, "ZnO – Nanostructures, Defects, and Devices," *Materials Today* 10, no. 5 (May 2007): 40–48, https://doi.org/10.1016/s1369-7021(07)70078-0.

17. F. Fabbri, M. Villani, A. Catellani, A. Calzolari, G. Cicero, and D. Calestani, "Zn Vacancy Induced Green Luminescence on Non-Polar Surfaces in ZnO Nanostructures," *Scientific Reports* 4, no. 1 (June 2014), https://doi.org/10.1038/srep05158.

18. Z. L. Wang, "Zinc Oxide Nanostructures: Growth, Properties and Applications," *Journal of Physics: Condensed Matter* 16, no. 25 (June 2004): R829–R858, https://doi.org/10.1088/0953-8984/16/25/r01.

19. J. Goldberger, D. J. Sirbuly, M. Law, and P. Yang, "ZnO Nanowire Transistors," *The Journal of Physical Chemistry B* 109, no. 1 Dec. 2004): 9–14, https://doi.org/10.1021/jp0452599.

20. P. Ghamgosar, F. Rigoni, S. You, et al., "ZnO-Cu_2O core-shell nanowires as stable and fast response photodetectors, "*Nano Energy* 51(2018): 308–316, https://doi.org/10.1016/j.nanoen.2018.06.058.

21. M. Izaki, T. Ohta, M. Kondo, T. Takahashi, F. B. Mohamad, and M. Zamzuri, "Electrodeposited ZnO-Nanowire/Cu_2O Photovoltaic Device with Highly Resistive ZnO Intermediate Layer," *ACS Applied Materials and Interfaces* 6, no. 16 Aug. 2014): 13461–13469.

22. P. Ghamgosar, F. Rigoni, M. G. Kohan, S. You, E. A. Morales, and R. Mazzaro, "Self-Powered Photodetectors Based on Core–Shell ZnO–Co_3O_4 Nanowire Heterojunctions," *ACS Applied Materials and Interfaces* 11, no. 26 (June 2019): 23 454–23 462, https://doi.org/10.1021/acsami.9b04838.

23. I. Dobryden, R. Borgani, F. Rigoni, P. Ghamgosar, I. Concina, and N. Almqvist, "Nanoscale Characterization of an All-Oxide Core–Shell Nanorod Heterojunction using Intermodulation Atomic Force Microscopy (AFM) Methods," *Nanoscale Advances* 3, no. 15 (2021): 4388–4394, https://doi.org/10.1039/d1na00319d.

24. M. Patel, M. Kumar, H.-S. Kim, W.-H. Park, E. H. Choi, and J. Kim, "Reactive Sputtering Growth of co3o4 Thin Films for All Metal Oxide Device: a Semitransparent and Self-Powered Ultraviolet Photodetector," *Materials Science in Semiconductor Processing* 74 Feb. 2018): 74–79, https://doi.org/10.1016/j.mssp.2017.09.018.

25. A. Tahira, Z. H. Ibupoto, A. Nafady, M. Willander, and O. Nur, "Efficient and Stable co3o4/ZnO Nanocomposite for Photochemical Water Splitting," *Journal of Cluster Science* 33, no. 1 Jan. 2021): 387–394, https://doi.org/10.1007/s10876-021-01980-2.

26. B. Kupfer, K. Majhi, D. A. Keller, Y. Bouhadana, S. Rühle, and H. N. Barad, "Thin Film Co_3O_4/TiO_2 Heterojunction Solar Cells," *Advanced Energy Materials* 5, no. 1 Aug. 2014): 1401007, https://doi.org/10.1002/aenm.201401007.

27. Y. Yang, W. Cheng, and Y. F. Cheng, "Preparation of co3o4@ZnO Core-Shell Nanocomposites with Intrinsic P-N Junction as High-Performance Photoelectrodes for Photoelectrochemical Cathodic Protection under Visible Light," *Applied Surface Science* 476 (May 2019): 815–821, https://doi.org/10.1016/j.apsusc.2019.01.157.

28. T.-M. Tien and E. L. Chen, "A Novel zno/co3o4 Nanoparticle for Enhanced Photocatalytic Hydrogen Evolution under Visible Light Irradiation," *Catalysts* 13, no. 5 (2023), https://www.mdpi.com/2073-4344/13/5/852.

29. S. Z. Bisri, S. Shimizu, M. Nakano, and Y. Iwasa, "Endeavor of Iontronics: From Fundamentals to Applications of Ion-Controlled Electronics," *Advanced Materials* 29, no. 25 (June 2017): 1607054, https://doi.org/10.1002/adma.201607054.

30. D. Prete, V. Demontis, V. Zannier, M. J. Rodriguez-Douton, L. Guazzelli, and F. Beltram, "Impact of Electrostatic Doping on Carrier Concentration and Mobility in InAs Nanowires," *Nanotechnology* 32, no. 14 Jan. 2021): 145204, https://doi.org/10.1088/1361-6528/abd659.

31. H. Yoo, Y. H. Lee, M.-G. Lee, and J.-Y. Sun, "Gel-Based Ionic Circuits," *Chemical Reviews* 125, no. 18 Sept. 2025): 8956–9011, https://doi.org/10.1021/acs.chemrev.5c00245.

32. C. Cao, M. Melegari, M. Philippi, D. Domaretskiy, N. Ubrig, and I. Gutiérrez-Lezama, "Full Control of Solid-State Electrolytes for Electrostatic Gating," *Advanced Materials* 35, no. 18 (Mar. 2023), https://doi.org/10.1002/adma.202211993.

33. V. Demontis, D. Prete, E. Faella, F. Giubileo, V. Zannier, and O. Durante, "Persistent Polarization Effects and Memory Properties in Ionic-Liquid Gated InAs Nanowire Transistors," *Nano Express* 5, no. 3 (July 2024): 035007, https://doi.org/10.1088/2632-959X/ad6581.

34. Y. Ma, C.-F. Xu, X.-R. Mao, Y. Wu, J. Yang, and L.-P. Xu, "Oriented Self-Assembly of Hierarchical Branch Organic Crystals for Asymmetric Photonics," *Journal of the American Chemical Society* 145, no. 16 Apr. 2023): 9285–9291, https://doi.org/10.1021/jacs.3c02061.

35. H. Lin, Y. Ma, S. Chen, and X. Wang, "Hierarchical Integration of Organic Core/Shell Microwires for Advanced Photonics," *Angewandte Chemie International Edition* 62, (2023): e202214214, https://doi.org/10.1002/anie.202214214.

36. Y. Shi, Q. Lv, Y. Tao, Y. Ma, and X. Wang, "Design and Growth of Branched Organic Crystals: Recent Advances and Future Applications," *Angewandte Chemie International Edition* 61, (2022): e202208768, https://doi.org/10.1002/anie.202208768.

37. Y. Tao, S. Peng, X. Wang, Z. Li, X. Zhang, and L. Liao, "Sequential Self-Assembly of 1D Branched Organic Homostructures with Optical Logic Gate Function," *Advanced Functional Materials* 28, no. 48 Oct. 2018): 1804915, https://doi.org/10.1002/adfm.201804915.

38. Z. Ye, H. He, and L. Jiang, "Co-Doping: an Effective Strategy for Schieving Stable P-Type Zno Thin Films," *Nano Energy* 52 Oct. 2018): 527–540, https://doi.org/10.1016/j.nanoen.2018.08.001.

39. A. M. Lord, T. G. Maffeis, A. S. Walton, D. M. Kepaptsoglou, Q. M. Ramasse, and M. B. Ward, "Factors that Determine and Limit the Resistivity of High-Quality Individual ZnO Nanowires," *Nanotechnology* 24, no. 43 Oct. 2013): 435706, https://doi.org/10.1088/0957-4484/24/43/435706.

40. L. J. Brillson and Y. Lu, "ZnO Schottky Barriers and Ohmic Contacts," *Journal of Applied Physics* 109, no. 12 (June 2011): 121301, https://doi.org/10.1063/1.3581173.

41. N. Sinha, G. Ray, S. Godara, M. K. Gupta, and B. Kumar, "Enhanced Piezoelectric Output Voltage and Ohmic Behavior in Cr-Doped ZnO Nanorods," *Materials Research Bulletin* 59 Nov. 2014): 267–271, https://doi.org/10.1016/j.materresbull.2014.07.032.

42. B. S. Sannakashappanavar, A. B. Yadav, V. Kumar, N. V. L. N. Murty, and K. Singh, "Low Resistance Ohmic Contact On ZnO Thin Film Revealed by Schottky Barrier Height," *Silicon* 14, no. 4 Jan. 2021): 1531–1536, https://doi.org/10.1007/s12633-021-00949-0.

43. A. Grillo and A. D. Bartolomeo, "A Current–Voltage Model for Double Schottky Barrier Devices," *Advanced Electronic Materials* 7, no. 2 Dec. 2020): 2000979, https://doi.org/10.1002/aelm.202000979.

44. K. J. Rietwyk, D. A. Keller, K. Majhi, A. Ginsburg, M. Priel, and H.-N. Barad, "High-Throughput Electrical Potential Depth-Profiling in Air," *Advanced Materials Interfaces* 4, no. 16 (June 2017): 1700136, https://doi.org/10.1002/admi.201700136.

45. D. R. Lide, ed., *CRC Handbook of chemistry and physics*, 89th ed. (Boca Raton, FL: CRC Press, June 2008).

46. B. Varghese, B. Mukherjee, K. R. G. Karthik, K. B. Jinesh, S. G. Mhaisalkar, and E. S. Tok, "Electrical and Photoresponse Properties of Co_3O_4 Nanowires," *Journal of Applied Physics* 111, no. 10 (May 2012): 104306, https://doi.org/10.1063/1.4712497.

47. D. K. Schroder, *Semiconductor material and device characterization*, 3rd ed. (ser. Wiley - IEEE, Chichester, England: Wiley-Blackwell, Jan. 2006).

48. P. Wang, X. Zhao, and B. Li, "ZnO-Coated CuO Nanowire Arrays: Fabrications, Optoelectronic Properties, and Photovoltaic Applications," *Optics Express* 19, no. 12 (June 2011): 11 271–11 279.

49. T. Cossuet, J. Resende, L. Rapenne, O. Chaix-Pluchery, C. Jiménez, and G. Renou, "Zno/cucro2 Core–Shell Nanowire Heterostructures for Self-Powered UV Photodetectors with Fast Response," *Advanced Functional Materials* 28, no. 43 Sept. 2018): 1803142, https://doi.org/10.1002/adfm.201803142.

50. D. Prete, J. Lieb, V. Demontis, L. Bellucci, V. Tozzini, and D. Ercolani, "III-V Semicondutor Nanostructures and Iontronics: InAs Nanowire-Based Electric Double Layer Field Effect Transistors," in *15th International Conference on Concentrator Photovoltaic Systems (CPV-15)* (AIP Publishing, 2019).

51. K. Xu and S. K. Fullerton-Shirey, "Electric-Double-Layer-Gated Transistors Based on Two-Dimensional Crystals: recent Approaches and Advances," *Journal of Physics: Materials* 3, no. 3 (May 2020): 032001, https://doi.org/10.1088/2515-7639/ab8270.

52. O. Game, U. Singh, T. Kumari, A. Banpurkar, and S. Ogale, "Zno(n)–Spiro-Meotad Hybrid Photodiode: an Efficient Self-Powered Fast-Response UV (Visible) Photosensor," *Nanoscale* 6 (2014): 503–513, https://doi.org/10.1039/C3NR04727J.